High-Frequency Modelling of Constant On-Time Current Mode Buck Converter and Controller Design by Combining Genetic Algorithm

Xiangpeng Cheng, *Student Member, IEEE*, Jinjun Liu, *Fellow, IEEE*, Yu Shao, *Student Member, IEEE*, and Zeng Liu, *Member, IEEE*

***Abstract*—Constant on-time current mode (COTCM) Buck converters are widely used in power management integrated circuit (ICs) for microprocessors. Small-signal models are necessary tools to design high-quality controllers. Existing models neglect output voltage ripples (OVRs) and spectrum extension caused by switching, which makes significant errors under high control bandwidth. This article adopts Fourier series to describe OVRs precisely. Then, influences of OVRs on COTCM are analyzed. Finally, spectrum coupling from current loop and voltage loop is incorporated to obtain a high-frequency model, and four universal analytical expressions in frequency domain are obtained with the aid of matrix calculation. Based on the proposed model and genetic algorithm, an optimal controller design method is developed. Simulation and experiment validate the accuracy of proposed model and the effectiveness of proposed design method.**

***Index Terms*—Buck converter, constant on-time current mode (COTCM), genetic algorithm (GA), high-frequency model, spectrum coupling.**

I. Introduction

CONSTANT on-time control, compared with constant frequency control, features high light-load efficiency, which becomes a mandate for CPU power supplies [1]. There are mainly two widely-used schemes, i.e., ripple-based constant on-time (RBCOT) [2] and constant on-time current mode (COTCM) [3]. RBCOT is distinguished by circuit simplicity due to only utilizing output voltage feedback. However, it suffers from instability when adopting capacitors with low equivalent series resistance (ESRs) [4]. Although adding virtual inductor current can solve this issue, the control simplicity is sacrificed [5]. COTCM feeds back inductor current directly to support system stability. Besides, current mode naturally owns easy paralleling of multiple converters and easy adjustment of adaptive voltage positioning [6]. These advantages make COTCM buck converters popular in power management integrated circuit (ICs) for microprocessors [7], [8], [9].

Small-signal models are necessary tools to design high-quality controllers. Ridley's model successfully represents the "sample and hold" effect of peak current mode by a transfer function, which is the key to predict subharmonic oscillations [10]. However, it's unreasonable to extend it to COTCM [11], since the "sample and hold" effect does not exist in variable frequency control. Two high-frequency models have been proposed to analyze current-loop successfully. Li model treats power plant and modulator as a single entity, which is further analyzed by describing function [12]. While Yan model treats power plant and modulator as different parts, and uses sampled-data model to consider spectrum coupling of current-loop [13]. Both models can explain natural stability of current-loop, and closed-loop transfer functions predicted by them are equivalent with each other. Unfortunately, voltage-loop is out of consideration in them. Voltage-loop will introduce output voltage ripples (OVRs) and extended spectrum caused by switching, and most of them can be filtered out under low control bandwidth. However, high control bandwidth is beneficial for enhancing dynamic response and reducing capacitor's volume of power supplies [14], [15], which is more and more important with the increase of CPU's integration level [16]. OVRs and spectrum coupling of voltage-loop become significant under high control bandwidth, where Li model and Yan model fail due to neglect of them.

Recently, OVRs and spectrum coupling have been both incorporated into modeling process to derive high-frequency models for constant frequency voltage-mode (VM) control. OVRs will create modulation waveform ripples (MWRs) through feedback control. According to mathematical characteristics of MWRs at crossing points, they are divided into two types, i.e., differentiable type and nondifferentiable type. Two models have been proposed for VM Buck converters with differentiable MWRs [17], [18]. They explain influences of MWRs by their derivatives at crossing points, which is verified by Taylor-series expansion. Another two models have been proposed for VM Buck converters with nondifferentiable MWRs. One claims that influences of MWRs are depended on their left derivatives at crossing points, which is built on a premise that infinite sideband components have been considered [19]. The other one claims that influences are equivalent to the average of left and right derivatives of

Manuscript received 13 March 2022; revised 28 June 2022; accepted 25 July 2022. Date of publication 10 August 2022; date of current version 6 September 2022. This work was supported by the National Natural Science Foundation of China under Grant 51437007. Recommended for publication by Associate Editor S. Mishra. *(Corresponding author: Jinjun Liu.)*

The authors are with the State Key Laboratory of Electrical Insulation and Power Equipment, School of Electrical Engineering, Xi'an Jiaotong University, Xi'an 710049, China (e-mail: alexcheng1994@163.com; jjliu@mail.xjtu.edu.cn; 1159943091@qq.com; zengliu@mail.xjtu.edu.cn).

Color versions of one or more figures in this article are available at https://doi.org/10.1109/TPEL.2022.3197768.

Digital Object Identifier 10.1109/TPEL.2022.3197768

MWRs at crossing points, which only requires finite dominant sideband components [20].

Analyses of variable frequency control are much more challenging than constant frequency control. Additionally, not only voltage-loop, but also current-loop in COTCM contributes to spectrum coupling, which further complicates the modeling. Till now, research of high-frequency models for COTCM with voltage-loop is still far from perfection. Actually, COTCM is always stable without voltage-loop, which plays a main role to threat system stability [21]. This article aims to propose a high-frequency model for COTCM buck converters with voltage-loop. Influences of OVRs on COTCM are revealed through geometrical analyses and area equivalence principle. Spectrum coupling from voltage-loop and current-loop is incorporated to obtain an accurate small-signal model, and four universal analytical expressions in frequency domain are obtained with the aid of matrix calculation. A quantitative guidance is proposed to choose dominant OVRs harmonics and sideband components.

The high-frequency model is inevitably complicated by considering OVRs and spectrum coupling, which makes it difficult to design controller trough traditional pole-zero analyses. Recently, intelligent algorithms are introduced into controller designs for solving optimization problems [22], [23], [24]. Among them, genetic algorithm (GA) is outstanding for its powerful random search ability [25]. It does not require structural and gradient information of system, and has strong global search capabilities [25]. Researchers usually use a combination of GA and simulation to optimize the controller parameters [26], [27]. Although simulation can effectively judge the fitness of possible designs generated by GA, it is always time-consuming. Fortunately, the high-frequency model is an accurate analytical model, which can judge the fitness accurately and efficiently. Therefore, an optimal controller design method is proposed by combining the proposed model with GA.

Steady-state system ripples are analyzed in Section II by Fourier series. In Section III, transfer function of COTCM is derived by incorporating OVRs. Section IV introduces the high-frequency model. Section V describes the optimal controller design method. Section VI verifies the proposed model and design method by simulations and experiments. Conclusions is described in Section VII. In this article, capital letters indicate steady-state quantities, and small letters indicate perturbed-state quantities.

II. Steady-State Analyses for System Ripples

Accuracy of small-signal models highly depends on accuracy of corresponding steady-state analyses. First, the mechanism of COTCM buck converters is introduced. Then, system ripples in steady-state are analyzed by Fourier series.

A. Introduction of COTCM Buck Converters

A COTCM Buck converter is shown in Fig. 1. R, L, C, and R_c represent the load resistor, the inductor, the capacitor, and the ESR of capacitor. C_{c1}, C_{c2}, R_{c1}, and a transconductance G_m build the compensator. R_i is the sensing gain of inductor current i_L and v_i represents the sensed signal. $\tilde{v}_p$ is the small-signal perturbation for small-signal modeling.

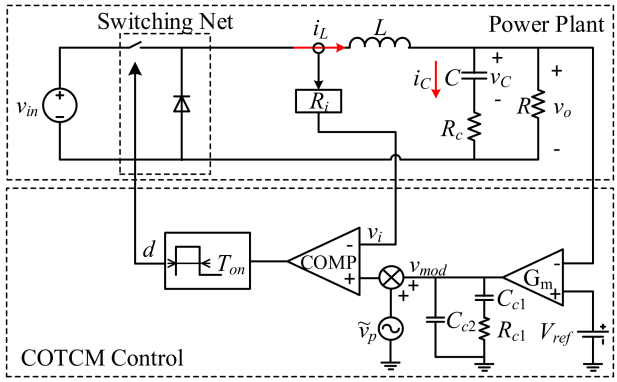

Fig. 1. COTCM Buck converter.

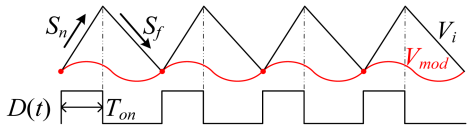

Fig. 2. $\hat{V}_{\rm mod}$ with differentiable crossing points.

The output voltage v_o is fed back to the compensator to create the modulation waveform $v_{\rm mod}$, which is compared with v_i to trigger the constant on-time controller to generate the control signal d. When $v_{\rm mod}$ intersects with v_i, the switch is turned on for a constant on-time T_{on}. Then, the switch is turned off until next intersection. The detailed structure of constant on-time controller can be found in [28].

B. Fourier Series of OVRs and MWRs

$\hat{V}_o$ represents steady-state OVRs, which are composed of capacitor and ESR voltage ripples. $\hat{V}_o$ contains harmonics with integer multiples of switching frequency f_s. Different types of MWRs ($\hat{V}_{\rm mod}$) are generated by filtering $\hat{V}_o$ through different compensator designs [20]. High-order compensators are widely-used to restrain high-frequency noises and compensate phase margin. They work as low-pass filters to remove majority of high-frequency harmonics, which makes $\hat{V}_{\rm mod}$ differentiable at crossing points as shown in Fig. 2. Here, S_n and S_f represent steady-state rising and falling slopes of V_i, and $D(t)$ represents the steady-state control signal.

As a periodic signal, $D(t)$ is expanded by Fourier series as

$$D(t)=\sum_{n=-\infty}^{+\infty}\frac{1-e^{-j2nD\pi}}{j2n\pi}e^{jn\omega_s t} \tag{1}$$

where D represents the steady-state duty ratio.

The transfer function of power plant filter is derived as

$$G_{vd}(s)=\frac{\tilde{v}_o(s)}{\tilde{d}(s)}=\frac{V_{\rm in}R_{\rm sum}(s)}{R_{\rm sum}(s)+sL} \tag{2}$$

where $R_{\rm sum}(s)$ is represented as

$$R_{\rm sum}(s)=\frac{(1+sCR_c)R}{1+sC(R+R_c)}. \tag{3}$$

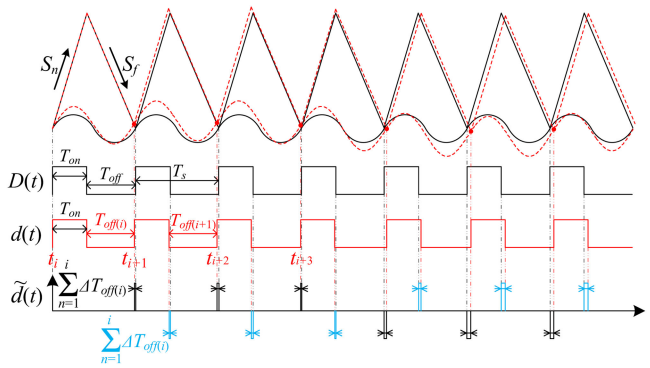

Fig. 3. Working mechanism of COTCM under small-signal perturbation.

By applying $G_{vd}(s)$ on necessary harmonics of $D(t)$, $\hat{V}_o$ can be derived as

$$\hat{V}_o(t) = \sum_{\substack{n=-k \\ n\neq 0}}^{+k} G_{vd}\left(jn\omega_s\right) \frac{1-e^{-j2nD\pi}}{j2n\pi} e^{jn\omega_s t} \tag{4}$$

where k represents the required harmonic order. How to decide k will be introduced in Section IV.

A single zero, double poles compensator is utilized in this article, whose transfer function is derived as

$$H_v\left(s\right) = \frac{g_m}{C_{c2}} \frac{s + 1/\left(R_{c1}C_{c1}\right)}{s\left[s + \left(C_{c1}+C_{c2}\right)/\left(R_{c1}C_{c1}C_{c2}\right)\right]} \tag{5}$$

where g_m represents the dc gain of $\mathrm{G_m}$.

By applying $H_v(s)$ on each harmonic of $\hat{V}_o$, $\hat{V}_{\mathrm{mod}}$ can be derived as

$$\hat{V}_{\mathrm{mod}}\left(t\right) = -\sum_{\substack{n=-k \\ n\neq 0}}^{+k} H_v\left(jn\omega_s\right) G_{vd}\left(jn\omega_s\right) \times \frac{1-e^{-j2nD\pi}}{j2n\pi} e^{jn\omega_s t}. \tag{6}$$

III. Transfer Function of COTCM

The transfer function of COTCM describes the relationship between modulation perturbation $\tilde{v}_p$ and control perturbation $\tilde{d}$. $\tilde{v}_p$ is defined as

$$\tilde{v}_p\left(t\right) = V_p \sin\left(\omega_p t - \theta_p\right) \tag{7}$$

where V_p, ω_p, and θ_p are the amplitude, frequency, and phase angle. $\tilde{v}_p$ is added to steady-state MWRs to form perturbated MWRs. Fig. 3 shows the working mechanism of perturbated COTCM. Red dashed lines represent the perturbated MWRs and sensed current signal, where crossing points move slightly under perturbation.

Here, T_{off} and T_s represent the steady-state off-time and steady-state cycle period; $T_{\mathrm{off}(i)}$ and $\Delta T_{\mathrm{off}(i)}$ represent the off-time and off-time perturbation of i_{th} cycle; t_i represent the start of i_{th} cycle as shown in

$$t_i = \left(i-1\right)T_s + \sum_{n=1}^{i-1} \Delta T_{\mathrm{off}(n)}. \tag{8}$$

S_n and S_f can be calculated as (9) and (10), where influences of input voltage perturbation $\tilde{v}_{\mathrm{in}}$ and output voltage perturbation $\tilde{v}_o$ are not considered

$$S_n\left(t\right) = R_i \frac{V_{\mathrm{in}}\left(t\right) - V_o\left(t\right)}{L} = \underbrace{R_i \frac{\left(1-D\right)V_{\mathrm{in}}}{L}}_{S_{n\_\mathrm{dc}}} - R_i \frac{\hat{V}_o\left(t\right)}{L} \tag{9}$$

$$S_f\left(t\right) = R_i \frac{V_o\left(t\right)}{L} = \underbrace{R_i \frac{DV_{\mathrm{in}}}{L}}_{S_{f\_\mathrm{dc}}} + R_i \frac{\hat{V}_o\left(t\right)}{L}. \tag{10}$$

Peak point amplitude of sensed current signal can be derived from the start or end of each cycle, and both results should be equal

$$\tilde{v}_p\left(t_i\right) + \hat{V}_{\mathrm{mod}}\left(t_i\right) + \int_{t_i}^{t_i+T_{\mathrm{on}}} S_n\left(t\right) dt = \tilde{v}_p\left(t_{i+1}\right) + \hat{V}_{\mathrm{mod}}\left(t_{i+1}\right) + \int_{t_i+T_{\mathrm{on}}}^{t_{i+1}} S_f\left(t\right) dt. \tag{11}$$

Two approximations are utilized to make a simplification

$$\hat{V}_{\mathrm{mod}}\left(t_{i+1}\right) \approx \hat{V}_{\mathrm{mod}}\left(t_i\right) + \hat{V}'_{\mathrm{mod}}\left(iT_s\right)\Delta T_{\mathrm{off}(i)} \tag{12}$$

$$\int_{t_i}^{t_{i+1}} \hat{V}_o\left(t\right) dt \approx \int_{t_i}^{t_i+T_s} \hat{V}_o\left(t\right) dt + \hat{V}_o\left(t\right)\Delta T_{\mathrm{off}(i)} = \hat{V}_o\left(t\right)\Delta T_{\mathrm{off}(i)}. \tag{13}$$

Equation (11) can be simplified as

$$\tilde{v}_p\left(t_i\right) - \tilde{v}_p\left(t_{i+1}\right) \approx \left(S_{f\_\mathrm{dc}} + S_c\right)\Delta T_{\mathrm{off}(i)} \tag{14}$$

where S_c is the sum of S_{c1} and S_{c2} as shown in (15). S_{c1} represents the influence of OVRs from voltage-loop, and S_{c2} represents the influence of OVRs from current-loop. Although S_{c2} is much smaller than S_{c1}, it's necessary to be considered for preventing parametric sensitivity in low-frequency domain, which will be explained in Section IV.

$$S_c = \underbrace{\hat{V}'_{\mathrm{mod}}\left(iT_s\right)}_{S_{c1}} + \underbrace{\frac{R_i}{L}\hat{V}_o\left(iT_s\right)}_{S_{c2}}$$

$$S_{c1} = -\sum_{\substack{n=-k \\ n\neq 0}}^{+k} H_v\left(jn\omega_s\right) G_{vd}\left(jn\omega_s\right) f_s\left(1-e^{-j2nD\pi}\right)$$

$$S_{c2} = \frac{R_i}{L}\sum_{\substack{n=-k \\ n\neq 0}}^{+k} G_{vd}\left(n\omega_s\right) \frac{1-e^{-j2nD\pi}}{j2n\pi}. \tag{15}$$

Based on (14), it's found that

$$\sum_{n=1}^{i} \Delta T_{\mathrm{off}(n)} = \sum_{n=1}^{i} \frac{\tilde{v}_p\left(t_i\right) - \tilde{v}_p\left(t_{i+1}\right)}{S_{f\_\mathrm{dc}} + S_c} = \frac{-\tilde{v}_p\left(t_{i+1}\right)}{S_{f\_\mathrm{dc}} + S_c}. \tag{16}$$

A switching-frequency sampling signal of $\tilde{v}_p$ is denoted as

$$\tilde{v}_p^*\left(t\right) = \sum_{i=1}^{+\infty} \tilde{v}_p\left(t\right)\delta\left(t - iT_s\right). \tag{17}$$

As shown in Fig. 3, $\tilde{d}$ is the control signal perturbation composed of narrow rectangles, which can be assumed as a series of pulses according to area equivalence principle

$$\tilde{d}(t) \approx \sum_{i=1}^{+\infty} \left[\left(\sum_{n=1}^{i} \Delta T_{\text{off}(n)} \right) \left(\delta\left(t - iT_s - T_{\text{on}}\right) - \delta\left(t - iT_s\right) \right) \right]. \tag{18}$$

By substituting (16) and (17) into (18), $\tilde{d}$ is reorganized as

$$\tilde{d}(t) = \frac{\tilde{v}_p^*(t) - \tilde{v}_p^*(t - T_{\text{on}})}{S_{f\_\text{dc}} + S_c}. \tag{19}$$

Equation (19) is further transferred to s-domain

$$\tilde{d}(s) = \underbrace{\frac{1 - e^{-sT_{\text{on}}}}{S_{f\_\text{dc}} + S_c}}_{F_m(s)} \tilde{v}_p^*(s). \tag{20}$$

$\hat{V}_{\text{mod}}$ will be larger with the increase of system bandwidth. Then, S_c is possible to be even larger than S_{f_dc}. Through increasing S_{f_dc} by adding R_i or reducing $\hat{V}_o$ by adding capacitor value, influences of S_c will be attenuated. While adding R_i and capacitor value will also decrease system bandwidth. In order to obtain high-bandwidth design, dc gain of compensator has to be increased, which further increases S_c. As a conclusion, S_c is significant for high-bandwidth design.

IV. Accurate Small-Signal Model

First, influences of input and output voltage perturbations on COTCM is derived. Then, it is extended to be an accurate small-signal model by incorporating spectrum coupling from voltage loop and current loop, and four universal analytical expressions in frequency domain are obtained. Finally, A quantitative guidance is proposed to choose dominant OVRs harmonics and sideband components.

A. Influences of Input and Output Voltage Perturbations

$\tilde{v}_{\text{in}}$ and $\tilde{v}_o$ will also influence current-loop by disturbing S_n and S_f. Transfer functions from $\tilde{v}_{\text{in}}$ and $\tilde{v}_o$ to $\tilde{d}$ can be derived as (21) and (22) by similar methods in Section III. Detailed process can be found in Appendix.

$$\begin{cases} \tilde{d}(s) = \underbrace{\dfrac{1 - e^{-sT_{on}}}{\left(S_{f\_dc} + S_c\right)\left(1 - e^{sT_s}\right)}}_{G_2(s)} \tilde{v}_{\text{ind}}^*(s) \\ \tilde{v}_{\text{ind}}(s) = \underbrace{-\dfrac{R_i\left(1 - e^{sT_{\text{on}}}\right)}{sL}}_{G_1(s)} \tilde{v}_{\text{in}}(s) \end{cases} \tag{21}$$

$$\begin{cases} \tilde{d}(s) = F_m(s)\, \tilde{v}_{od}^*(s) \\ \tilde{v}_{od}(s) = \underbrace{\dfrac{R_i}{sL}}_{H_i(s)} \tilde{v}_o(s) \end{cases}. \tag{22}$$

Additionally, $\tilde{v}_{\text{in}}$ will also influence the system through power plant, which is equivalent to (23) by open-loop analyses.

$$\tilde{d}(t) = \frac{D(t)\,\tilde{v}_{\text{in}}(t)}{V_{\text{in}}} = \sum_{n=-\infty}^{+\infty} \frac{1 - e^{-j2nD\pi}}{j2n\pi V_{\text{in}}} e^{jn\omega_s t} \tilde{v}_{\text{in}}(t). \tag{23}$$

Equation (23) is further transferred to s-domain

$$\tilde{d}(s) = \sum_{n=-\infty}^{+\infty} \frac{1 - e^{-j2nD\pi}}{j2n\pi V_{\text{in}}} \tilde{v}_{\text{in}}(s - jn\omega_s). \tag{24}$$

B. Considering Spectrum Coupling

Relationships between different input perturbations and control perturbation have been fully described by (20)–(24), where $\tilde{v}_p^*(s)$, $\tilde{v}_{\text{ind}}^*(s)$ and $\tilde{v}_{od}^*(s)$ represent ideal sampling signals in s-domain; $D(t)\tilde{v}_{\text{in}}(t)$ represents a nonideal sampling signal. When the system is perturbated by $\tilde{v}_p(\omega_p)$, $\tilde{v}_{\text{in}}(\omega_p)$, and $\tilde{v}_o(\omega_p)$, those sampling signals will generate spectrum extension with integer multiples of f_s, i.e., $\tilde{d}(\omega_p)$, $\tilde{d}(\omega_p \pm \omega_s)$, $\tilde{d}(\omega_p \pm 2\omega_s)$, $\tilde{d}(\omega_p \pm 3\omega_s)$, etc. These sideband components will flow through the voltage and current feedback to perturbate COTCM again. Next-generation sideband components will overlap with the last-generation to cause spectrum coupling.

The transfer function of open-loop output impedance is derived as

$$Z_o(s) = \frac{\tilde{v}_o(s)}{\tilde{i}_o(s)} = R_{\text{sum}}(s) // sL. \tag{25}$$

Combined (2) and (20)–(25), an accurate small-signal model considering spectrum coupling can be obtained as shown in Fig. 4, where $H_i(j\omega)$ is generated by (22). Relationships between input perturbations and extended spectrum can be derived as (26) and (27) by applying sampling theory on (20)–(21)

$$\frac{\tilde{d}(\omega + n\omega_s)}{\tilde{v}_{p2}(\omega)} = f_s F_m\left(j\left(\omega + n\omega_s\right)\right) n \in Z \tag{26}$$

$$\frac{\tilde{d}(\omega + n\omega_s)}{\tilde{v}_{\text{in}}(\omega)} = \frac{1 - e^{-j2nD\pi}}{j2n\pi V_{\text{in}}} + f_s G_1(j\omega)\, G_2\left(j\left(\omega + n\omega_s\right)\right). \quad n \in Z \tag{27}$$

C. Four Universal Analytical Expressions

Loop gain without considering spectrum coupling is derived as (28) by ignoring dashed lines in Fig. 4

$$T_{sf}(j\omega) = f_s F_m(j\omega)\, G_{vd}(j\omega)\left(H_v(j\omega) - H_i(j\omega)\right). \tag{28}$$

$T_{\text{sum}}(j\omega)$ is defined as

$$T_{\text{sum}}(j\omega) = \sum_{n=-k}^{k} T_{sf}\left(j\left(\omega + n\omega_s\right)\right). \tag{29}$$

As shown in Fig. 4, sideband components make each signal as a vector, and each transfer section as a matrix. Therefore, the proposed model can be transformed into a vector-matrix form in Fig. 5, where $\boldsymbol{S}_1$ and $\boldsymbol{S}_2$ represent spectrum extension matrixes; $\boldsymbol{G}_{vd}$ represents power plant filter matrix; $\boldsymbol{H}_v$ and $\boldsymbol{H}_i$ represent

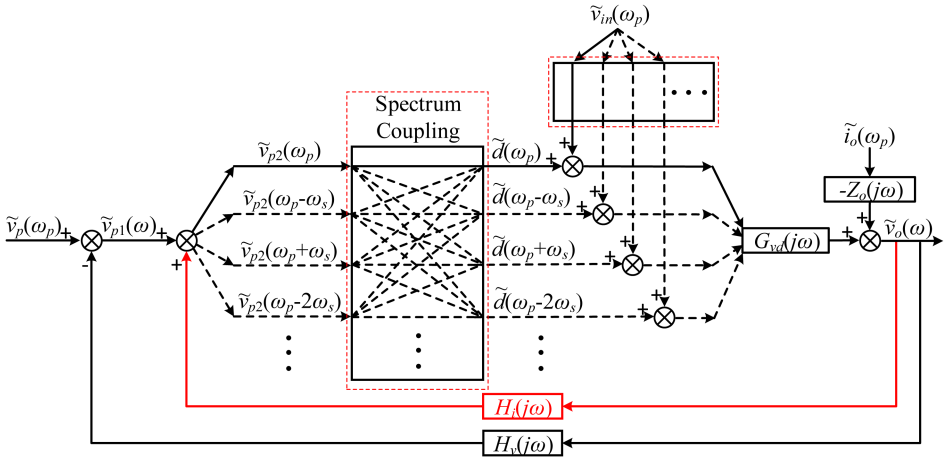

Fig. 4. High-frequency model of Buck converters.

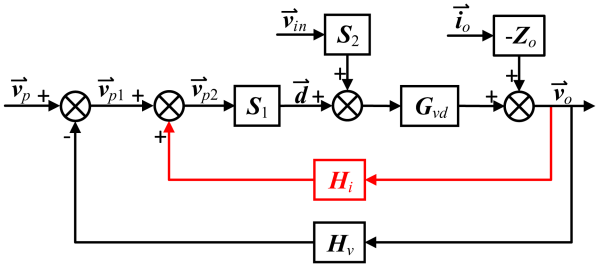

Fig. 5. Simplified model by vectors and matrixes.

voltage and current feedback matrixes. Each element of $\boldsymbol{S}_1$ and $\boldsymbol{S}_2$ can be obtained from (26) and (27); $\boldsymbol{G}_{vd}$, $\boldsymbol{Z}_o$, $\boldsymbol{H}_v$, and $\boldsymbol{H}_i$ are diagonal matrixes, diagonal elements can be obtained from $G_{vd}(j\omega)$, $Z_o(j\omega)$, $H_v(j\omega)$ and $H_i(j\omega)$ at corresponding frequency. With the aid of matrix calculation, four universal analytical expressions can be derived as follows.

Loop gain of voltage loop

$$T_{hf}\left(j\omega_p\right)=\frac{T_{sf}\left(j\omega_p\right)}{\left(1-\frac{H_i(j\omega_p)}{H_v(j\omega_p)}\right)\left(1+T_{\text{sum}}\left(j\omega_p\right)\right)-T_{sf}\left(j\omega_p\right)}. \tag{30}$$

Audio susceptibility, (31) shown at the bottom of this page.

Output impedance

$$Z_{o\_hf}\left(j\omega_p\right)=\frac{Z_o\left(j\omega_p\right)}{1+T_{hf}\left(j\omega_p\right)}. \tag{32}$$

Input impedance

$$Z_{in\_hf}\left(j\omega_p\right)\approx\frac{1}{\frac{DG_{hf}(j\omega_p)}{R_{\text{sum}}(j\omega_p)}+\frac{DV_{\text{in}}G_{hf}(j\omega_p)}{RG_{vd}(j\omega_p)}-\frac{D^2}{R}}. \tag{33}$$

Equation (33) is an approximative expression, which is built on an averaged relationship [29] as follows:

$$\tilde{i}_g\left(t\right)=D\tilde{i}_L\left(t\right)+\frac{DV_{\text{in}}}{R}\tilde{d}\left(t\right) \tag{34}$$

where $\tilde{i}_g$ represents input current. All of (30)–(33) include (29), where $T_{sf}(j(\omega_p+n\omega_s))$ corresponds to the selected sideband component one by one. How to decide the non-negative integer k will be introduced in following section.

D. Quantitative Guidance to Choose k

Frequency domain characteristics below f_s are capable of judging stability and designing controller for buck converters. Therefore, ω_p in (30)–(33) is limited as $0\sim\omega_s$. As shown in (28), $T_{sf}(j\omega)$ is the product of transfer functions of power plant filter and feedback loop, which is similar as a low-pass filter. Amplitude of $T_{sf}(j(\omega_p+n\omega_s))$ increases when $|\omega_p+n\omega_s|$ decreases, which means the corresponding sideband component more considerable.

A quantitative choice strategy of dominant sideband components based on experiences is proposed to reach a modeling balance between accuracy and simplicity: calculate $T_{sf}(j\omega)$ under $k=1$; as shown in Fig. 6, find the maximum solution $\omega_{\max}$ to make $|T_{sf}(j\omega)|$ equivalent to -20 dB; defined k as round($\omega_{\max}/\omega_s$). Other sideband components are ignored due to limited influences on the model's accuracy.

An important premise should be declared for this strategy: the selected order of OVRs harmonics should also be k; $T_{sf}(j(\omega_p+k\omega_s))$; and $T_{sf}(j(\omega_p-k\omega_s))$ should always be chosen together. This premise is used to prevent parametric sensitivity in low-frequency domain of (30) and (31). The denominator of

$$G_{hf}\left(j\omega_p\right)=\left(\frac{D}{V_{\text{in}}}+f_sG_1\left(j\omega_p\right)G_2\left(j\omega_p\right)\right)G_{vd}\left(j\omega_p\right)$$
$$-\frac{G_{vd}\left(j\omega_p\right)F_m\left(j\omega_p\right)}{1+T_{\text{sum}}\left(j\omega_p\right)}\sum_{n=-k}^{k}\left[\left(\frac{1-e^{-j2nD\pi}}{j2n\pi V_{\text{in}}}+f_sG_1\left(j\omega_p\right)G_2\left(j\left(\omega_p+n\omega_s\right)\right)\right)\times\frac{T_{sf}\left(j\left(\omega_p+n\omega_s\right)\right)}{F_m\left(j\left(\omega_p+n\omega_s\right)\right)}\right]. \tag{31}$$

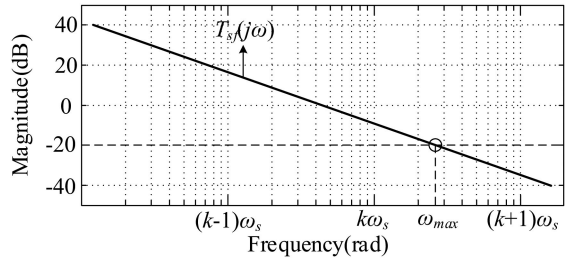

Fig. 6. Quantitative choice of *k*.

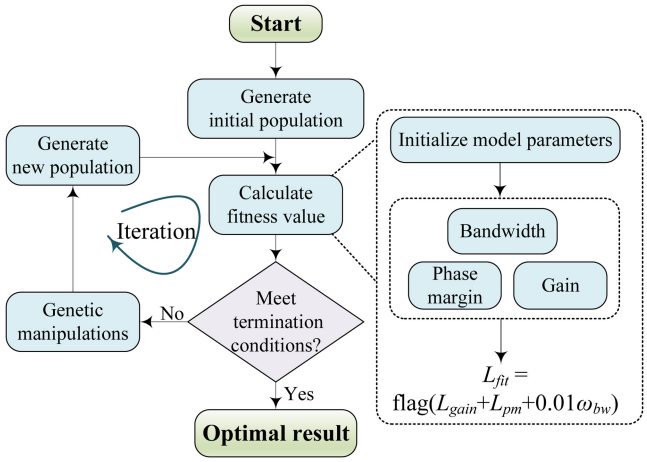

Fig. 7. Optimal controller design process.

(30) can be calculated as (35) with the aid of (15) when ω_p converges toward 0. It shows that in low-frequency domain, the value of the denominator is almost 0. If $T_{sf}[j(\omega_p\text{-}(k\text{+}1)\omega_s)]$is added into modelling as the choice strategy proposed in [18], [19] and [20] for constant frequency control, or the selected order of OVRs harmonics is not *k*, (35) would fail to converge to 0 in low-frequency domain

$$\lim_{\omega_p\to 0}\left[\left(1-\frac{H_i\left(j\omega_p\right)}{H_v\left(j\omega_p\right)}\right)\left(1+T_{\text{sum}}\left(j\omega_p\right)\right)-T_{sf}\left(j\omega_p\right)\right]$$
$$=\lim_{\omega_p\to 0}\left[\left(1-\frac{H_i\left(\omega_p\right)}{H_v\left(\omega_p\right)}\right)\left(\frac{S_c}{S_{f\_\text{dc}}+S_c}+\frac{-S_{c1}-S_{c2}}{S_{f\_dc}+S_c}\right)\right]=0. \tag{35}$$

The proposed model would be extremely accurate if infinite OVRs harmonics and sideband components are incorporated into modelling, where *k* should be infinite. Under this condition, (35) is still true. Therefore, the true value of the denominator in low-frequency domain should be closed to 0, and tiny prediction errors would cause huge deviations in (30). Similar analyses can be applied on the numerator of (31). That's why this premise should be strictly followed.

V. Optimal Controller Design Based on GA

The optimal controller design process is shown in Fig. 7, which is introduced step by step as follows.

Step 1: Generate an initial population.

First, the transfer function of controller in (5) can be transformed into pole-zero form

$$H_v\left(s\right)=\frac{\omega_1}{s}\frac{1+s/\omega_z}{1+s/\omega_p} \tag{36}$$

where ω_1, ω_z, and ω_p are parameters waiting to be optimized, and defined as genes in GA. These genes are combined to form an individual *A*

$$A=\left\{\omega_1,\omega_z,\omega_p\right\}. \tag{37}$$

Values of genes are generated by applying random function on their own ranges, and an initial population *P* can be produced by repeating this manipulation *N* times

$$A_k=\left\{\omega_{1\_k},\omega_{z\_k},\omega_{p\_k}\right\}\qquad k=1,2,\cdots N$$
$$P=\left\{A_1,A_2,\cdots A_N\right\}. \tag{38}$$

Step 2: Build fitness function and calculate individual fitness.

To judge individual fitness, fitness function is necessary. There are three key indicators of loop gain reflecting control qualities [30], which are used to form fitness function as follows.

1) ω_{bw} represents the bandwidth of loop gain. The larger ω_{bw} is, the faster the dynamic response is.
2) L_{pm} represents the phase margin of loop gain. The larger L_{pm} is, the better the stability of system is. It's derived as
$$L_{pm}=\text{angle}\left(T_{hf}\left(j\omega_{bw}\right)\right)+180^{\text{o}}. \tag{39}$$
3) L_{gain} represents the low-frequency amplitude of loop gain. The larger L_{gain} is, the higher the steady-state accuracy of system is. The amplitude of loop gain at 10 Hz is used
$$L_{\text{gain}}=20\log\left|T_{hf}\left(j20\pi\text{rad/s}\right)\right|. \tag{40}$$

Therefore, the fitness function is built as

$$L_{fit}=\text{flag}\left(L_{\text{gain}}+L_{pm}+0.01\omega_{bw}\right)$$
$$\text{flag}=\begin{cases}1 & L_{pm}\geq 30^o\\ 0 & L_{pm}<30^\circ\ or\ \omega_{bw}>0.5\omega_s\end{cases} \tag{41}$$

where sign function flag is used to guarantee enough phase margin larger than 30° and limit the bandwidth according to Sampling Theory. The larger L_{fit} is, the better the corresponding individual matches control requirements. ω_{bw} is the major part of L_{fit}, which means the control design wants dynamic response as faster as possible under stability.

Step 3: Decide whether termination conditions are met.

By calculating L_{fit} of all individuals in *P*, the average fitness of *P* can be obtained, which is denoted as $L_{\text{fit\_av}}$. $L_{\text{fit\_av}}$ of initial population is usually small, which will reach saturation after several iterations. Then, the optimal design with largest L_{fit} can be picked from *P*. Before saturation, Step 4 should be used to evolve *P* to increase L_{fit_av}. In this article, iteration times *M* are set as 15 to guarantee saturation.

Step 4: Carry out genetic manipulations.

To speed up the optimization process, several individuals with large L_{fit} in *P* are reserved to the next generation. Then select, cross and mutate other individuals in *P* [31].

TABLE I
PARAMETERS OF COTCM BUCK CONVERTER

Parameter	Value	Parameter	Value
V_{in}/V	20	R/Ω	1
V_o/V	5	R_i	0.0035
T_{on}/μs & f_s/ kHz	0.96 & 260	ω_1	1.07×10^4
L/μH	4	ω_z	4.54×10^4
C/μF	120	ω_p	4.00×10^5
R_c/mΩ	55		

1) *Selection*: Selection probability is calculated as follows:

$$p_k = \frac{L_{\text{fit\_}k}}{\sum_{k=1}^{N} L_{\text{fit\_}k}} \tag{42}$$

where $L_{\text{fit\_}k}$ represents the fitness of A_k, and p_k is the corresponding selection probability. Regions 0∼1 is divided into N parts, and length of each part depends on p_k. Individuals are chosen by generating random numbers between 0∼1. A_k with large $L_{\text{fit\_}k}$ owns large probability to be selected.

2) *Crossover*: Choose two individuals according to crossover rate p_{cross}, and randomly exchange parts of their genes. For example, A_i and A_j exchange their ω_z

$$\begin{aligned} A_i = \{\omega_{1\_i}, \omega_{z\_i}, \omega_{p\_i}\} \leftrightarrow A_j = \{\omega_{1\_j}, \omega_{z\_j}, \omega_{p\_j}\} \\ \downarrow \text{Nextgeneration} \\ A_i = \{\omega_{1\_i}, \omega_{z\_j}, \omega_{p\_i}\} \leftrightarrow A_j = \{\omega_{1\_j}, \omega_{z\_i}, \omega_{p\_j}\}. \end{aligned} \tag{43}$$

3) *Mutation*: To avoid local optimal solution and reach global optimization better, mutation is carried out on genes of several individuals according to mutation rate p_{mut}. For example, A_k is selected to mutate into

$$A_k = \{\text{rand}(\omega_1), \text{rand}(\omega_z), \text{rand}(\omega_p)\} \tag{44}$$

where rand represents the random function.

After genetic manipulations, a new population with higher $L_{\text{fit\_av}}$ will be produced, and better controller designs are obtained.

VI. VERIFICATIONS

In this Section, simulations and experiments are used to verify the accuracy of proposed model and the effectiveness of controller design method.

A. Verifications of Model Accuracy

The system in Fig. 1 is built in the SIMPLIS software, which performs small-signal ac analysis by a similar scheme in real measurements. Parameters are given in Table I.

Simulated waveforms of $\hat{V}_o$, $\hat{V}_{\text{mod}}$, and $R_i\times i_L$ are shown in Fig. 8, which indicates the system is stable. Amplitude-frequency characteristic of $T_{sf}(j\omega)$ under $k=1$ is obtained from (28) as shown in Fig. 9, where $f_{\max}$ is 607.2 kHz. Therefore, k equals to round($f_{\max}/f_s$) = 2. Then, S_{f_dc} and S_c are derived as 4.38×10^3 and 6.30×10^3 separately from (10) and (15). Under such high-bandwidth design, S_c is much larger than S_{f_dc}, which means influences of OVRs are significant for the system.

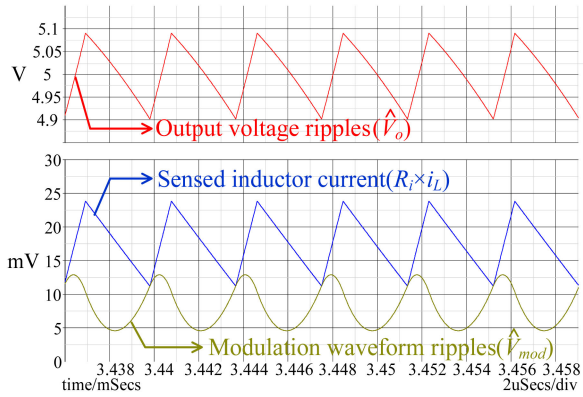

Fig. 8. Stable waveforms of $\hat{\boldsymbol{V}}_{\boldsymbol{o}}$, $\hat{\boldsymbol{V}}_{\boldsymbol{mod}}$, and $R_i\times i_L$ in simulation.

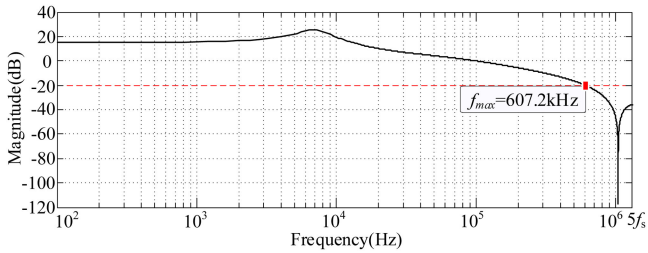

Fig. 9. Amplitude-frequency characteristic of $T_{sf}(j\omega)$ under $k=1$.

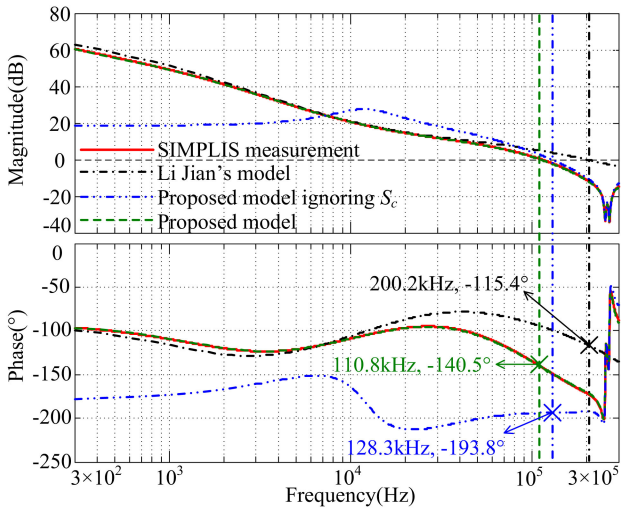

Fig. 10. Loop gain obtained by simulation and different models.

To show the accuracy of proposed model, frequency domain characteristics predicted by Li model, the proposed model ignoring S_c, and the proposed model are compared with simulated results.

As shown in Fig. 10, the loop gain predicted by Li model fails to predict magnitude attenuation and phase delay in high-frequency domain for ignorance of OVRs and spectrum coupling, which predicts an over-optimistic phase margin. The loop gain predicted by proposed model ignoring S_c still contains big errors, which predicts an over-pessimistic phase margin. It shows that just incorporating spectrum coupling into modelling is not enough. The loop gain predicted by proposed model (bandwidth:

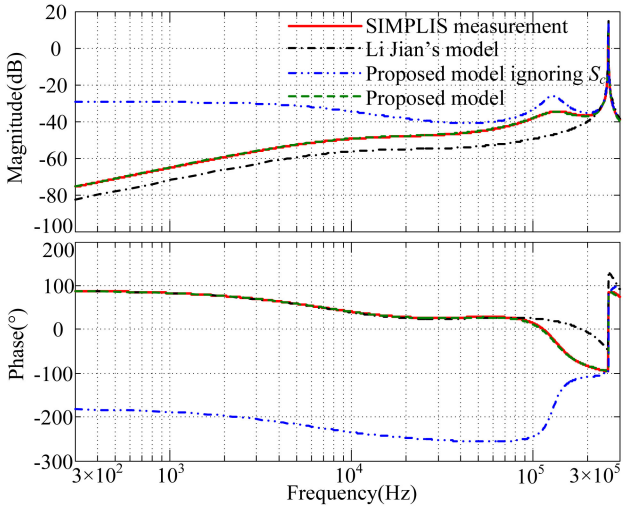

Fig. 11. Audio susceptibility obtained by simulation and different models.

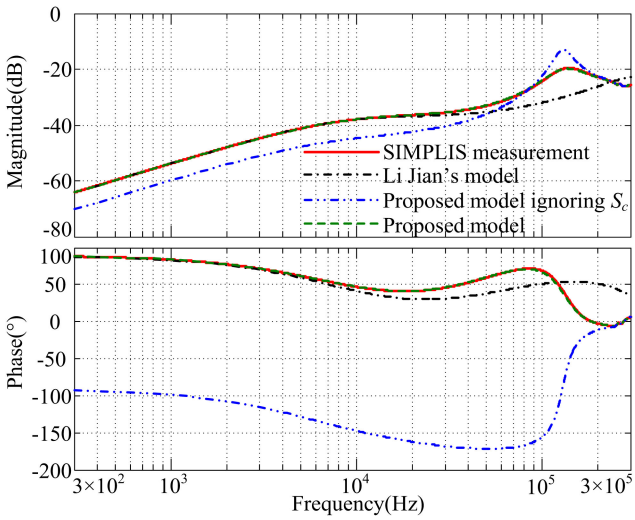

Fig. 13. Output impedance obtained by simulation and different models.

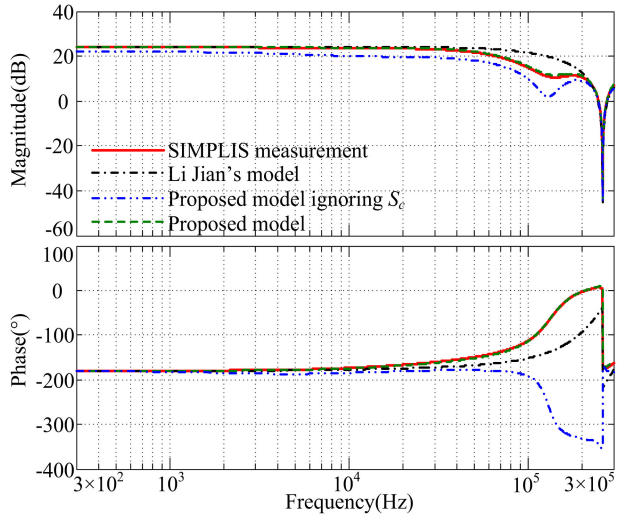

Fig. 12. Input impedance obtained by simulation and different models.

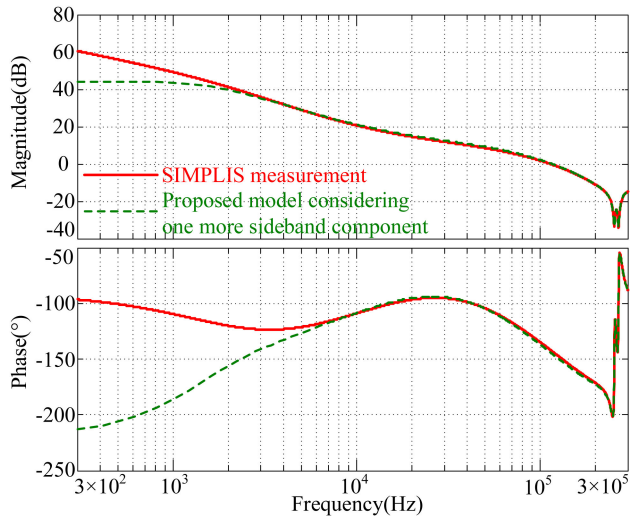

Fig. 14. Loop gain obtained by simulation and proposed model considering one more sideband component.

110.8 kHz and phase margin: 39.5°) matches well with the simulated result (bandwidth: 113.2 kHz and phase margin: 38.4°), which predicts system stability accurately.

Comparisons of audio susceptibility, input impedance, and output impedance are shown in Figs. 11–13. Similar as loop gain comparison, only the proposed model is accurate enough to reflect frequency domain characteristics.

As shown in Fig. 14, if one more sideband component, i.e., $T_{sf}(j(\omega_p\text{-}3\omega_s))$, is added in (29) to derive the loop gain, huge deviation between the theoretical result and simulated result will occur in low-frequency domain due to the parametric sensitivity of proposed model. The quantitative choice strategy of dominant sideband components proposed in Section IV should be strictly followed.

An experimental platform is built as shown in Fig. 15, whose parameters are the same as those in Table I except for $T_{\rm on}$. The real $T_{\rm on}$ is 0.945 μs and the corresponding f_s is 264.6 kHz. Experimental waveforms of $\hat{V}_o$, $V_{\rm in}\times d(t)$, and $\hat{V}_{\rm mod}$ are shown in Fig. 16, which indicates the system is stable. The loop gain is measured by the venable frequency analyzer as shown Fig. 17, which is almost the same as the theoretical result. Tiny deviations between them are mainly due to parameter variations, parasitic parameters and measurement errors in the real system. The measured bandwidth is 118.2 kHz and the measured phase margin is 29.8°.

When values of C and R_c in Table I are replaced as 50 μF and 4 mΩ, corresponding loop gains predicted by Li model and proposed model are shown in Fig. 18. Li model predicts the system should be stable. While the proposed model predicts negative phase margin, which means the system should be unstable. Experimental waveforms of $\hat{V}_o$ and $V_{\rm in}\times d(t)$ are shown in Fig. 19, where the pulse bursting phenomenon [4] occurs. It is clear that the proposed model successfully reflects instability of the system, while Li model fails.

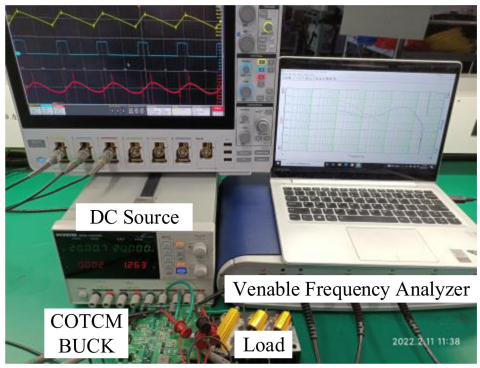

Fig. 15. Experimental platform.

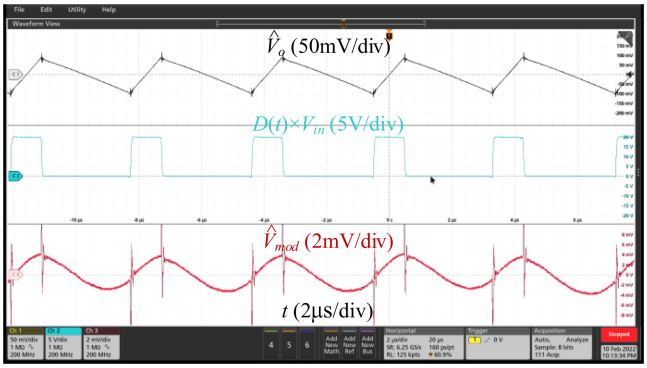

Fig. 16. Experimental waveforms in stable case: CH 1, $\hat{V}_o$; CH 2, $V_{\text{in}}\times d(t)$; and CH 3, $\hat{V}_{\text{mod}}$.

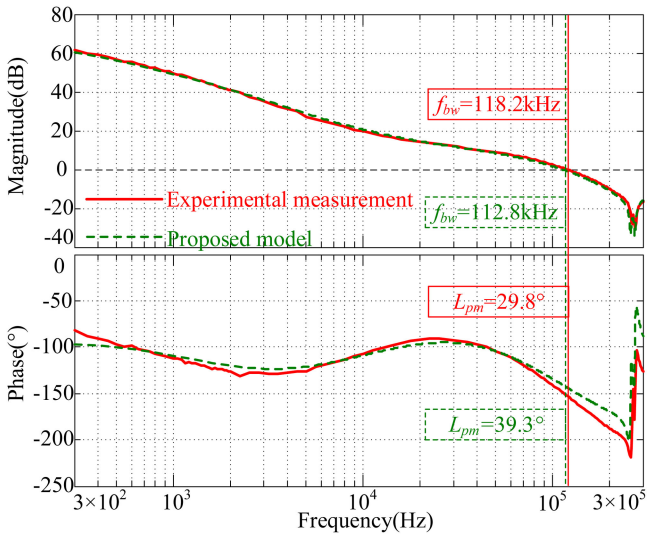

Fig. 17. Loop gain obtained by experiment and proposed model.

B. Verifications of Effectiveness of Optimal Controller Design

In last part, when C and R_c in Table I are replaced as 50 μF and 4 mΩ, the system falls into instability. Therefore, the proposed optimal controller design method is used to move the system back into stability.

Firstly, ranges of ω_1, ω_z, and ω_p are defined. ω_{bw} is set as $\omega_s/3 = 5.44\times10^5$ to obtain a high-bandwidth design; ω_z is placed before resonant frequency ($1/\sqrt{\text{LC}}$) of power plant to improve system phase margin, which is defined as $\omega_z\in(0,7.1\times10^4)$; ω_p is placed in high-frequency domain to attenuate noises and limited under $10\omega_{bw}$, which is defined as $\omega_p\in(0,5.4\times10^6)$; ω_1 can be calculated with the aid of Li model under $\omega_z = 7.1\times10^4$ and $\omega_p = 5.4\times10^6$, which is derived as $\omega_1 = 6.8\times10^3$. Then, ranges of ω_1 is defined as $\omega_1\in(0,6.8\times10^4)$.

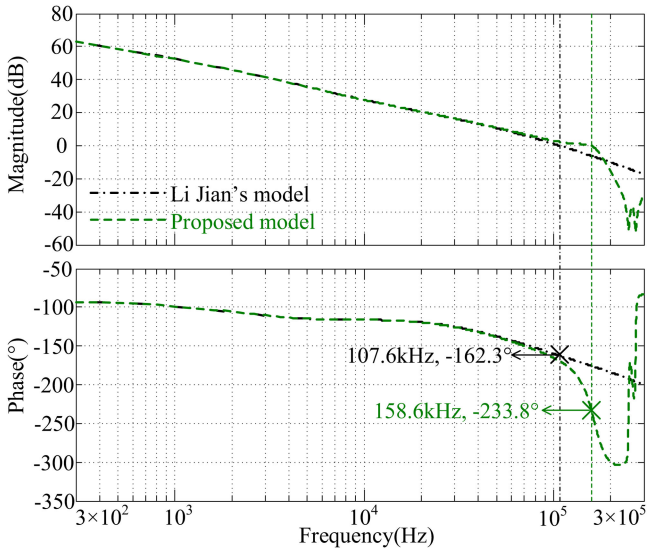

Fig. 18. Loop gain obtained by Li model and proposed model.

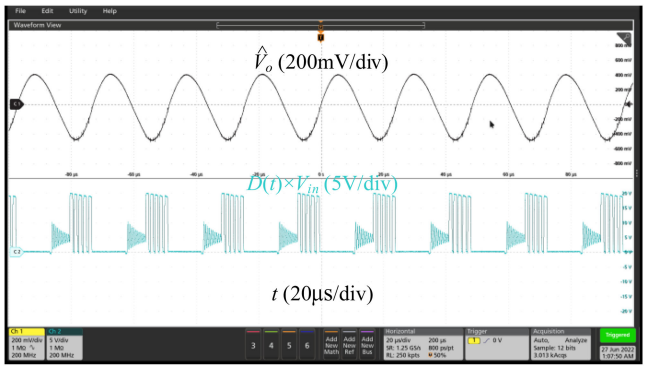

Fig. 19. Experimental waveforms in unstable case: CH 1, $\hat{V}_o$ and CH 2, $V_{\text{in}}\times d(t)$.

TABLE II
PARAMETERS OF GENETIC ALGORITHM

Parameter	Value	Parameter	Value
Population size N	100	Range of ω_1	$(0,6.8\times10^4)$
Generation number M	15	Range of ω_z	$(0,7.1\times10^4)$
Crossover rate p_{cross}	0.9	Range of ω_p	$(0,5.4\times10^6)$
Mutation rate p_{mut}	0.1		

Parameters of GA is given in Table II.

Optimal controller design process shown in Fig. 7 is achieved with the aid of MATLAB, and fitness is calculated by using (30) and (41). The variation of $L_{\text{fit\_av}}$ in optimal process is shown in Fig. 20. When iteration times reach 12, $L_{\text{fit\_av}}$ is closed to saturation, and $M = 15$ is a conservative choice. The

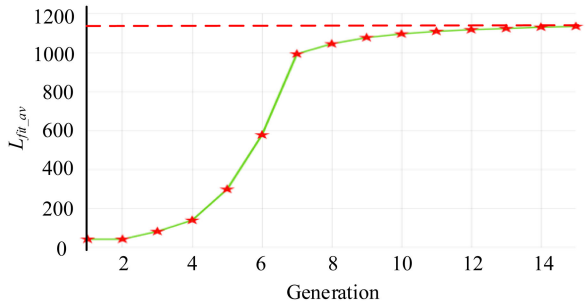

Fig. 20. Saturation process of average fitness value.

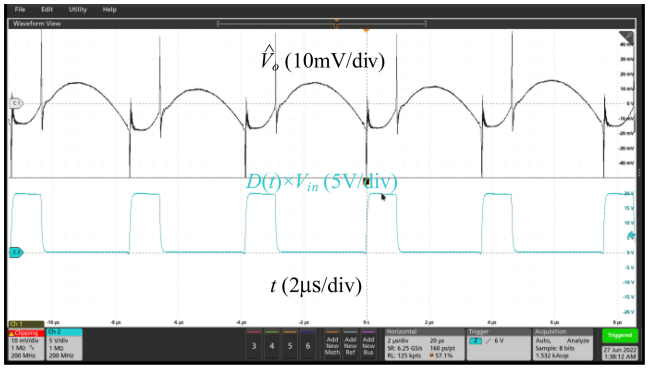

Fig. 21. Experimental waveforms under optimal controller design: CH 1, $\hat{V}_o$ and CH 2, $V_{\text{in}}\times d(t)$.

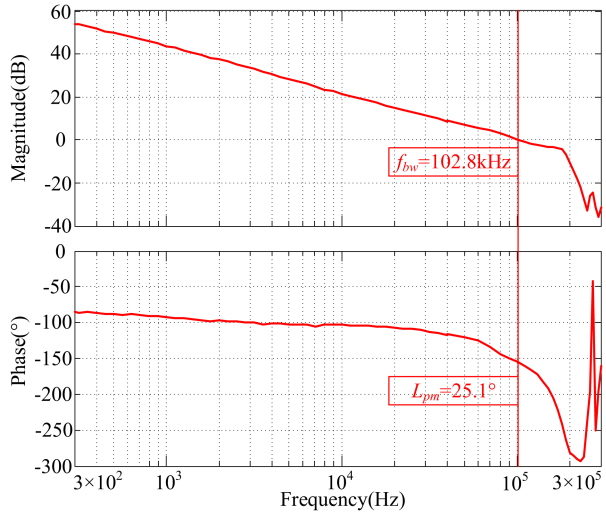

Fig. 22. Experimental loop gain under optimal controller design.

largest L_{fit} of individual among all populations is 1141, and the corresponding genes are $\omega_1 = 4.46\times10^3$, $\omega_z = 3.66\times10^4$, and $\omega_p = 1.11\times10^6$. This individual represents the optimal design result, and the optimization process costs only 63s, which shows the high efficiency of proposed method.

Experimental waveforms under the optimal design is shown in Fig. 21. It is clear that system works stably. The measured loop gain is shown in Fig. 22. Corresponding bandwidth and phase margin are 102.8 kHz and 25.1°, which achieves a stable high-bandwidth design. In experiment, there exists a parasitic capacitance around G_{m}, which equivalently increase C_{c2} of controller in (5) and moves the pole of controller slightly lower. That is why experimental phase margin is a little lower than the design limitation (30°).

The scheme proposed in [26] is also adopted to tune controller parameters, which combines GA with simulation to find optimal design. The simulation time of Simulink is set to 50 ms; the fitness function is designed as the absolute-error integration of time-domain variables; parameters of GA is the same with Table II for fair comparison. In each iteration, the calculation of L_{fit} is based on the simulated result of circuit, which is time-consuming. The optimal design result is $\omega_1 = 5.75\times10^3$, $\omega_z = 6.28\times10^4$, and $\omega_p = 2.19\times10^6$. Simulated bandwidth and phase margin are 80.1 kHz and 50.3°, which also achieves a stable high-bandwidth design. While using the same computer, the optimization time is around 3.2 h, which is around 200 times larger than the proposed method.

VII. Conclusion

This article proposes a high-frequency model for COTCM buck converters. Fourier series is utilized to describe steady-state OVMs and MWRs precisely. Transfer functions of COTCM incorporating OVRs reveal that influences of system ripples are decided by the derivative of MWRs and the value of OVRs at steady-state crossing points. The accurate small-signal model is derived by considering spectrum coupling from voltage and current loop, and transfer functions of loop gain, audio susceptibility, input impedance and output impedance are obtained based on it. A quantitative guidance with a boundary of -20 dB is used to choose dominant sideband components. An optimal controller design method is proposed by combining this model with GA, which features high-accuracy and high-efficiency. All these conclusions have been verified with simulations and experiments.

Appendix

1) Transfer function from $\tilde{v}_{\text{in}}$ to $\tilde{d}$

$\tilde{v}_{\text{in}}$ is defined as

$$\tilde{v}_{\text{in}}(t) = V_p \sin(\omega_p t - \theta_p). \tag{A1}$$

$\tilde{v}_{ind}$ is defined as

$$\tilde{v}_{\text{ind}}(t) = \frac{R_i}{\omega_p L}\left[\tilde{v}_{\text{in}}\left(t+\frac{\pi}{2\omega_p}\right) - \tilde{v}_{\text{in}}\left(t+T_{\text{on}}+\frac{\pi}{2\omega_p}\right)\right]. \tag{A2}$$

Based on the geometrical relationship of sensed current signal, it's found that

$$\hat{V}_{\text{mod}}(t_i) + \int_{t_i}^{t_i+T_{\text{on}}}\left[S_n(t) + \frac{R_i}{L}\tilde{v}_{\text{in}}(t)\right]dt = \hat{V}_{\text{mod}}(t_{i+1}) + \int_{t_i+T_{\text{on}}}^{t_{i+1}} S_f(t)\,dt \tag{A3}$$

which can be simplified as

$$\tilde{v}_{\text{ind}}(t_i) \approx (S_{f\_\text{dc}} + S_c)\,\Delta T_{\text{off}(i)}. \tag{A4}$$

A switching-frequency sampling signal of $\tilde{v}_{\text{ind}}$ is defined as

$$\tilde{v}^*_{\text{ind}}(t) = \sum_{i=1}^{+\infty} \tilde{v}_{\text{ind}}(t)\,\delta(t - iT_s) \tag{A5}$$

$\tilde{d}$ is assumed as (A6) according to area equivalence principle

$$\tilde{d}(t) \approx \sum_{i=1}^{+\infty} \left[\left(\sum_{n=1}^{i} \Delta T_{\text{off}(n)} \right) \left(\delta(t - iT_s - T_{\text{on}}) - \delta(t - iT_s) \right) \right]. \tag{A6}$$

Based on (A6), it's found that

$$\begin{aligned} &\tilde{d}(t) - \tilde{d}(t + T_s) \\ &\approx \sum_{i=1}^{+\infty} \Delta T_{\text{off}(i+1)} \delta(t - iT_s) \\ &\quad - \sum_{i=1}^{+\infty} \Delta T_{\text{off}(i+1)} \delta(t - iT_s - T_{\text{on}}). \end{aligned} \tag{A7}$$

By substituting (A4) and (A5) into (A7), it's reorganized as

$$\tilde{d}(t) - \tilde{d}(t + T_s) = \frac{\tilde{v}^*_{\text{ind}}(t) - \tilde{v}^*_{\text{ind}}(t - T_{\text{on}})}{S_{f\_\text{dc}} + S_c}. \tag{A8}$$

Equation (A8) is further transferred to s-domain

$$\begin{cases} \tilde{d}(s) = \frac{1 - e^{-sT_{\text{on}}}}{(S_{f\_\text{dc}} + S_c)(1 - e^{sT_s})} \tilde{v}^*_{\text{ind}}(s) \\ \tilde{v}_{\text{ind}}(s) = -\frac{R_i \left(1 - e^{sT_{\text{on}}}\right)}{sL} \tilde{v}_{\text{in}}(s) \end{cases}. \tag{A9}$$

2) Transfer function from $\tilde{v}_o$ to $\tilde{d}$

$\tilde{v}_o$ is defined as

$$\tilde{v}_o(t) = V_p \sin(\omega_p t - \theta_p) \tag{A10}$$

$\tilde{v}_{od}$ is defined as

$$\tilde{v}_{od}(t) = -\frac{R_i}{\omega_p L} \tilde{v}_o \left(t + \frac{\pi}{2\omega_p} \right). \tag{A11}$$

Based on the geometrical relationship of sensed current signal, it's found that

$$\begin{aligned} &\hat{V}_{\text{mod}}(t_i) + \int_{t_i}^{t_i + T_{\text{on}}} \left[S_n(t) - \frac{R_i}{L} \tilde{v}_o(t) \right] dt \\ &= \hat{V}_{\text{mod}}(t_{i+1}) + \int_{t_i + T_{\text{on}}}^{t_{i+1}} \left[S_f(t) + \frac{R_i}{L} \tilde{v}_o(t) \right] dt \end{aligned} \tag{A12}$$

which can be simplified as

$$\tilde{v}_{od}(t_i) - \tilde{v}_{od}(t_{i+1}) \approx (S_{f\_\text{dc}} + S_c)\,\Delta T_{\text{off}(i)}. \tag{A13}$$

Based on (A13), it's found that

$$\sum_{n=1}^{i} \Delta T_{\text{off}(n)} = \sum_{n=1}^{i} \frac{\tilde{v}_{od}(t_i) - \tilde{v}_{od}(t_{i+1})}{S_{f\_\text{dc}} + S_c} \approx \frac{-\tilde{v}_{od}(t_{i+1})}{S_{f\_\text{dc}} + S_c}. \tag{A14}$$

A switching-frequency sampling signal of $\tilde{v}_{od}$ is defined as

$$\tilde{v}^*_{od}(t) = \sum_{i=1}^{+\infty} \tilde{v}_{od}(t)\,\delta(t - iT_s). \tag{A15}$$

By substituting (A14) and (A15) into (A6), $\tilde{d}$ is reorganized as

$$\tilde{d}(t) = \frac{\tilde{v}^*_{od}(t) - \tilde{v}^*_{od}(t - T_{\text{on}})}{S_{f\_\text{dc}} + S_c}. \tag{A16}$$

Equation (A16) is further transferred to s-domain

$$\begin{cases} \tilde{d}(s) = \frac{1 - e^{-sT_{\text{on}}}}{S_{f\_\text{dc}} + S_c} \tilde{v}^*_{od}(s) \\ \tilde{v}_{od}(s) = \frac{R_i}{sL} \tilde{v}_o(s) \end{cases}. \tag{A17}$$

REFERENCES

[1] Voltage Regulator Module (VRM) and Enterprise Voltage Regulator-Down *(EVRD) 11.1*, Intel, Santa Clara, CA, USA, Sep. 2009.

[2] T. Qian, W. Wu, and W. Zhu, "Effect of combined output capacitors for stability of buck converters with constant on-time control," *IEEE Trans. Ind. Electron.*, vol. 60, no. 12, pp. 5585–5592, Dec. 2013.

[3] C. F. Nien et al., "A novel adaptive Quasi-constant on-time current-mode buck converter," *IEEE Trans. Power Electron.*, vol. 32, no. 10, pp. 8124–8133, Oct. 2017.

[4] J. Wang, J. Xu, and B. Bao, "Analysis of pulse bursting phenomenon in constant-on-time-controlled buck converter," *IEEE Trans. Ind. Electron.*, vol. 58, no. 12, pp. 5406–5410, Dec. 2011.

[5] C. J. Chen et al., "A novel ripple-based constant on-time control with virtual inductor current ripple for buck converter with ceramic output capacitors," in *Proc. 26th Annu. IEEE Appl. Power Electron. Conf. Expo.*, 2011, pp. 1488–1493.

[6] Y. J. Chen, D. Chen, Y. C. Lin, C.-J. Chen, and C.-H. Wang, "A novel constant on-time current-mode control scheme to achieve adaptive voltage positioning for DC power converters," in *Proc. IECON 38th Annu. Conf. IEEE Ind. Electron. Soc.*, 2012, pp. 104–109.

[7] LTC3812-5 datasheet, Analog Device, Wilmington, MA, USA, 2007, [Online]. Available: https://www.analog.com/media/en/technical-documentation/data-sheets/38125fc.pdf

[8] TPS51120 datasheet, Texas Instrum., Dallas, TX, USA, 015, [Online]. Available: https://www.ti.com.cn/cn/lit/ds/symlink/tps51120.pdf

[9] TPS51116 datasheet, Texas Instrum., Dallas, TX, USA, 2018, [Online]. Available: https://www.ti.com/lit/ds/symlink/tps51116.pdf

[10] R. B. Ridley, "A new, continuous-time model for current-mode control (power convertors)," *IEEE Trans. Power Electron.*, vol. 6, no. 2, pp. 271–280, Apr. 1991.

[11] R. B. Ridley, "A new continuous-time model for current-mode control with constant frequency, constant on-time, and constant off-time," in *Proc. 21st Annu. IEEE Conf. Power Electron. Specialists*, 1990, pp. 382–389.

[12] J. Li and F. C. Lee, "New modeling approach and equivalent circuit representation for current-mode control," *IEEE Trans. Power Electron.*, vol. 25, no. 5, pp. 1218–1230, May 2010.

[13] N. Yan, X. Ruan, and X. Li, "A general approach to sampled-data modeling for ripple-based control—Part II: Constant ON-Time and constant OFF-Time control," *IEEE Trans. Power Electron.*, vol. 37, no. 6, pp. 6385–6396, Jun. 2022.

[14] Y. Qiu, K. Yao, Y. Meng, M. Xu, F. C. Lee, and M. Ye, "Control-loop bandwidth limitations for multiphase interleaving buck converters," in *Proc. 19th Annu. IEEE Appl. Power Electron. Conf. Expo.*, 2004, pp. 1322–1328.

[15] A. Borrell, M. Castilla, J. Miret, J. Matas, and L. García de Vicuña, "Control design for multiphase synchronous buck converters based on exact constant resistive output impedance," *IEEE Trans. Ind. Electron.*, vol. 60, no. 11, pp. 4920–4929, Nov. 2013.

[16] D. James, "Moore's law continues into the 1x-nm era," in *Proc. 27th Annu. SEMI Adv. Semicond. Manuf. Conf.*, 2016, pp. 324–329.

[17] S. Hsiao, D. Chen, C. Chen, and H. Nien, "A new multiple-frequency small-signal model for high-bandwidth computer V-Core regulator applications," *IEEE Trans. Power Electron.*, vol. 31, no. 1, pp. 733–742, Jan. 2016.

[18] X. Cheng, J. Liu, and Z. Liu, "A generalized multifrequency small-signal model for high-bandwidth buck converters under constant-frequency voltage-mode control," *IEEE Trans. Power Electron.*, vol. 35, no. 8, pp. 8186–8199, Aug. 2020.

[19] X. Li, X. Ruan, Q. Jin, M. Sha, and C. K. Tse, "Small-Signal models with extended frequency range for DC–DC converters with large modulation ripple amplitude," *IEEE Trans. Power Electron.*, vol. 33, no. 9, pp. 8151–8163, Sep. 2018.
[20] X. Cheng, J. Liu, and Z. Liu, "Accurate small-signal modelling and stability analysis of wide-input buck converter considering modulation waveform ripples," *IEEE Trans. Power Electron.*, vol. 37, no. 6, pp. 6962–6971, Jun. 2022.
[21] Y. Chen, D. Chen, Y. Lin, C.-J. Chen, and C.-H. Wang, "A novel constant on-time current-mode control scheme to achieve adaptive voltage positioning for DC power converters," in *Proc. 38th Annu. Conf. IEEE Ind. Electron. Soc.*, 2012, pp. 104–109.
[22] M. Hung, L.-S. Shu, S.-J. Ho, S.-F. Hwang, and S.-Y. Ho, "A novel intelligent multiobjective simulated annealing algorithm for designing robust PID controllers," *IEEE Trans. Syst., Man, Cybern. Part A, Syst. Humans*, vol. 38, no. 2, pp. 319–330, Mar. 2008.
[23] G. Mühürcü, E. Kose, A. Muhurcu, and A. Kuyumcu, "Parameter optimization of PI controller by PSO for optimal controlling of a buck converter's output," in *Proc. Int. Artif. Intell. Data Process. Symp.*, 2017, pp. 1–6.
[24] S. Zhao, F. Blaabjerg, and H. Wang, "An overview of artificial intelligence applications for power electronics," *IEEE Trans. Power Electron.*, vol. 36, no. 4, pp. 4633–4658, Apr. 2021.
[25] S. Forrest, "Genetic algorithms, 'principles of natural selection applied to computation," *Science*, vol. 261, no. 5123, pp. 872–878, 1993.
[26] A. Divakar and J. Jacob, "Genetic algorithm based tuning of nonfragile and robust PI controller for PSFB DC-DC converter," in *Proc. Int. Conf. Commun. Electron. Syst.*, 2019, pp. 1846–1851.
[27] C. -C. Peng and C. -L. Lee, "Performance demands based servo motor speed control: A genetic algorithm proportional-integral control parameters design," in *Proc. Int. Symp. Comput., Consum. Control*, 2020, pp. 469–472.
[28] S. Zhen et al., "Transient response improvement of DC-DC converter by current mode variable on time control," in *Proc. IEEE 61st Int. Midwest Symp. Circuits Syst.*, 2018, pp. 603–606.
[29] R. D. Middlebrook and S. Cuk, "A general unified approach to modelling switching-converter power stages," in *Proc. IEEE Power Electron. Specialists Conf.*, 1976, pp. 18–34.
[30] W. E. Robert and M. Dragan, *Fundamentals of Power Electronics*. 2nd ed. New York, NY, USA: Kluer Acad. Publ., 2001.
[31] K. S. Kostov and J. J. Kyyra, "Genetic algorithm optimization of peak current mode controlled buck converter," in *Proc. IEEE Midnight-Summer Workshop Soft Comput. Ind. Appl.*, 2005, pp. 111–116.

Xiangpeng Cheng (Student Member, IEEE) received the B.S. degree in electrical engineering and automation in 2016 from Xi'an Jiaotong University, Xi'an, China, where he is currently working toward the Ph.D. degree in power electronics and electric drive.

His research interests include small-signal modeling theories for dc/dc converters, impedance modeling of grid-connected converters, stability analyses of multi-terminal dc transmission systems and intelligent optimization algorithm for control design.

Jinjun Liu (Fellow, IEEE) received the B.S. and Ph.D. degrees in electrical engineering from Xi'an Jiaotong University, Xi'an, China, in 1992 and 1997, respectively.

He was a Faculty with the XJTU Electrical Engineering School. From late 1999 to early 2002, he was with the Center for Power Electronics Systems, Virginia Polytechnic Institute and State University, Blacksburg, VA, USA, as a Visiting Scholar. In late 2002, he was a Full Professor and then the Head of the Power Electronics and Renewable Energy Center at XJTU, which now comprises more than 20 faculty members and more than 200 graduate students and carries one of the leading power electronics programs in China. From 2005 to early 2010, he was an Associate Dean of Electrical Engineering School, XJTU, and from 2009 to early 2015, the Dean for Undergraduate Education, XJTU. He is currently a XJTU Distinguished Professor of Power Electronics. He coauthored 3 books (including one textbook), published more than 500 technical papers in peer-reviewed journals and conference proceedings, holds more than 70 invention patents (China/US/EU), and delivered for many times plenary keynote speeches and tutorials at IEEE conferences or China national conferences. His research interests include modeling, control, and design methods for power converters and electronified power systems, power quality control and utility applications of power electronics, and micro-grids for sustainable energy and distributed generation.

Dr. Liu was the recipient of many times governmental awards at national level or provincial/ministerial level for scientific research/teaching achievements. He also the recipient of the 2006 Delta Scholar Award, the 2014 Chang Jiang Scholar Award, the 2014 Outstanding Sci-Tech Worker of the Nation Award, the 2016 State Council Special Subsidy Award, the IEEE TRANSACTIONS ON POWER ELECTRONICS 2016 and 2021 Prize Paper Awards, and the Nomination Award for the Grand Prize of 2020 Bao Steel Outstanding Teacher Award. He was the IEEE POWER ELECTRONICS SOCIETY REGION 10 Liaison and then China Liaison for ten years. Since 2006, has been an Associate Editor for the IEEE TRANSACTIONS ON POWER ELECTRONICS, 2015–2019 Executive Vice President and 2020–2021 Vice President of IEEE PELS. He was on the Board of China Electrotechnical Society 2012–2020 and was elected the Vice President in 2013 and the Secretary General in 2018 of the CES Power Electronics Society. He was the Vice President for International Affairs, China Power Supply Society from 2013 to 2021, and since 2016, the inaugural Editor-in-Chief of CPSS TRANSACTIONS ON POWER ELECTRONICS AND APPLICATIONS. He was elected the President of CPSS in November 2021. Since 2013, he has been the Vice Chair of the Chinese National Steering Committee for College Electric Power Engineering Programs.

Yu Shao (Student Member, IEEE) received the B.S. degree in electrical engineering and automation in 2021 from Xi'an Jiaotong University, Xi'an, China, where he is currently working toward the Master's degree in power electronics and electric drive.

His research interests include small-signal modeling theories for dc/dc converters, impedance modeling of grid-connected converters, stability analyses of multiterminal dc transmission systems and intelligent optimization algorithm for control design.

Zeng Liu (Member, IEEE) received the B.S. degree from Hunan University, Changsha, China, and the M.S. and Ph.D. degrees from Xi'an Jiaotong University (XJTU), Xi'an, China, in 2006, 2009, and 2013, respectively, all in electrical engineering.

He was a Faculty Member in electrical engineering with XJTU, where he is currently an Associate Professor. From 2015 to 2017, he was with the Center for Power Electronics Systems, Virginia Polytechnic Institute and State University, Blacksburg, VA, USA, as a Visiting Scholar. His research interests include control and stability of power electronics systems with multiple converters for renewable energy and energy storage applications.

Dr. Liu was the recipient of two Prize Paper Awards in IEEE TRANSACTIONS ON POWER ELECTRONICS. He is currently an Associate Editor for IEEE OPEN JOURNAL OF POWER ELECTRONICS and on the Editorial Board for the Energies, and served as Secretary-General for 2019 IEEE 10TH INTERNATIONAL SYMPOSIUM ON POWER ELECTRONICS FOR DISTRIBUTED GENERATION SYSTEMS and 2020 THE 4TH INTERNATIONAL CONFERENCE ON HVDC.